frontiers in Energy Research

ORIGINAL RESEARCH
published: 19 May 2021
doi: 10.3389/fenrg.2021.673923

Integrated Three-Dimensional Carbon Nanopolyhedron/Metal Sulfides: An Efficient Electrocatalyst Toward Oxygen Reduction Reaction

Yi-Wen Yang[1,2] *and Bing-Ye Song*[1,2]*

[1] School of Building Services Science and Engineering, Xi'an University of Architecture and Technology, Xi'an, China, [2] Key Laboratory of Thermo-Fluid Science and Engineering of MOE, School of Energy & Power Engineering, Xi'an Jiaotong University, Xi'an, China

OPEN ACCESS

Edited by:
Yuanzhen Chen,
Xi'an Jiaotong University, China

Reviewed by:
Sen Yao,
Henan Agricultural University, China
Zheng Miao,
North China Electric Power University, China
Jinfu Ma,
North Minzu University, China

***Correspondence:**
Bing-Ye Song
bysong@xauat.edu.cn

Specialty section:
This article was submitted to Electrochemical Energy Conversion and Storage, a section of the journal Frontiers in Energy Research

Received: 28 February 2021
Accepted: 13 April 2021
Published: 19 May 2021

Citation:
Yang Y-W and Song B-Y (2021) Integrated Three-Dimensional Carbon Nanopolyhedron/Metal Sulfides: An Efficient Electrocatalyst Toward Oxygen Reduction Reaction. Front. Energy Res. 9:673923. doi: 10.3389/fenrg.2021.673923

Carbon-based materials hybridized with metal sulfides have gained growing attention as catalytic materials for oxygen reduction reaction (ORR) due to their synergistic effects in terms of richer structural features and higher electrochemical activities. Here, a series of Zn/Co/Fe-based metal-organic frameworks (MOFs) as the precursors, which can be adopted as efficient ORR catalysts, were synthesized through a sulfuration–calcination treatment. The effects of precursor composition, heteroatom doping, and pyrolysis temperature on the structure and electrochemical performance of the catalysts were discussed in detail. It is found that well-grown carbon nanotubes (CNTs) on the surface of graphitic carbon matrix are formed under the synergy effect of trimetallic-based species during pyrolysis. Benefiting from the three-dimensional unique structure with appropriate dopants and high porosity, the catalyst derived from the optimized Zn/Co/Fe-MOFs achieves a half-wave potential of 0.87 V in an alkaline medium for ORR, which is comparable with commercial electrocatalysts. In addition, an outstanding ORR durability of the proposed catalyst in alkaline media was also demonstrated. This work highlights the potential to rationally design and fabricate high-performance ORR catalysts for commercialization.

Keywords: oxygen reduction reaction, metal sulfides, metal-organic frameworks, electrocatalyst, three-dimensional unique structure

INTRODUCTION

With the exhaustion of traditional fossil fuels, the demand for renewable energy and high-efficiency energy conversion technologies (such as electrolytic splitting of water and fuel cells) is increasingly becoming more urgent (Shabani et al., 2020). The oxygen reduction reaction (ORR) is the pivotal cathode reaction process in renewable energy technologies. Due to the sluggish kinetics of the ORR, commercial noble metal-based catalysts (such as Pt/C, Pd/C) are required to accelerate the processes (Katsounaros et al., 2014; Yu et al., 2017). Although noble metal-based materials

have been proven to be superior ORR catalysts, their prohibitive cost, scarcity in supply, and weak durability significantly prohibit their large-scale application (Yu et al., 2016; Fu et al., 2017). Accordingly, the exploration of more efficient and cost-effective non-noble metal ORR catalysts is imperative for the development of renewable energy technologies (Chung et al., 2017).

Over the past few decades, a large number of low-cost alternatives with ORR catalytic performance have been investigated as substitutes for noble metal-based catalysts (Zhang et al., 2015; Zhu et al., 2016). The transition metal oxide/sulfide and N-doped carbon (NC) hybrids have been proven to possess competitive catalytic activity for ORR in alkaline media, which is mainly attributed to the coupling effect between metal sulfides/oxides and carbon matrixes (Hu et al., 2016; Cheng et al., 2019). Recently, MOFs have been considered as one of the most promising precursors of nitrogen-doped carbon by virtue of the spatial ordered N-containing organic ligands and subsequent derived porous structures (Chen et al., 2015; Tang et al., 2015; Wang et al., 2019). Numerous studies have shown that nitrogen metal embedded into carbon are the active sites with desirable binding energy for O=O dissociation and O_2 adsorption/desorption for ORR (Zhao et al., 2013; Zhang et al., 2018).

Zhong et al. have developed a new 2D sandwich-like ZIF-8-derived graphene-based nitrogen-doped porous carbon sheets (GNPCSs) obtained by *in situ* growing ZIF-8 (zeolitic imidazolate framework, ZIF) on grapheme oxide (Zhong et al., 2014). Compared with commercial Pt/C catalysts, the GNPCSs show comparable onset potential, higher current density, and especially excellent tolerance to methanol and superior durability in the ORR. Those properties might be attributed to a synergistic effect between NC and graphene with regard to structure and composition. The core–shell-structured Co@Co_3O_4/NC composites are synthesized by carbonizing and oxidizing MOFs by Guo et al. (2018). This Co@Co_3O_4/NC composites exhibit excellent ORR performance and long-term stability, which can be attributed to the synergy between the Co bulk and Co_3O_4 (Guo et al., 2018). Also, the Co@Co_3O_4/NC composites are prepared via a similar two-step approach (carbonization and oxidation of Co-MOFs) by Qi et al. (2018). A large number of exposed active sites and the synergy between Co@Co_3O_4 and NC make it superior ORR catalyst (Qi et al., 2018). In addition to metal oxides, the construction of metal sulfides/carbon-based materials has gradually become a research hotspot in recent years. A series of Co-MOFs crystals with controllable structures and morphologies have been obtained via a solvent-controlled method by Liu et al. After a subsequent pyrolysis treatment, the Co_9S_8@SNCC composites are formed and they are proved to have excellent ORR catalytic activity and stability (Liu S. W. et al., 2017). Li et al. (2016) have developed a highly active and durable ORR electrocatalyst, Co/Co_9S_8/NPGC-800, by a pyrolysis procedure using the Co-chelated polyaniline (PANI) as the nitrogen and carbon sources. The composites show excellent activity and stability for ORR, which can be attributed to the appropriate proportion (Co/Co_9S_8) of the main active-constituents (Li et al., 2016). In spite of the great progress that has been achieved by monometallic MOFs (Zn-ZIF, Co-ZIF), there are still several issues (such as low conductivity, rare metal/nitrogen carbon synergy, limited active sites) that limit the ORR catalytic performance of the derived catalysts (Xia et al., 2016; Rui et al., 2018).

Accordingly, more and more scientific research are aimed at the catalysts derived from bimetallic or trimetallic MOFs. This is mainly due to the fact that the introduction of a second metal provides more opportunity to synthesize a larger variety of bimetallic MOFs with a tunable composition and an intrinsic structure compared with monometallic MOFs (Liu et al., 2008; Luo et al., 2019; Zhang et al., 2020). You et al. (2015) have proposed bimetal-organic frameworks self-adjusted synthesis of support-free porous Co–N–C catalysts by carbonizing Zn/Co bi-MOFs. The experimental results show that the presence of initial Zn forms a spatial isolation of Co that suppresses its sintering during the pyrolysis process, and Zn evaporation also promotes the surface area of the resultant catalysts (You et al., 2015). The optimal Co–N–C exhibits remarkable ORR activity with a half-wave potential of 0.871 V [vs. reversible hydrogen electrode (RHE)], excellent stability and methanol tolerance in 0.1 mol L^{-1} (0.1 M) KOH. Recently, Chen et al. (2017) have developed a highly active ORR catalyst: MO-Co@NC (NC, M = Zn or Co) via pyrolysis of CoZn-ZIF precursor. It is worth noting that the surface contents of pyridinic N for ORR and the surface contents of Co–N_x are enhanced, while the high specific surface areas, high porosity, and high electrochemical active surface areas are also achieved in the presence of Zn in the precursor. Unexpectedly, the optimized CoZn–NC-700 shows a high ORR activity and an excellent durability during the ORR process, even better than Pt/C.

In addition to Co–Zn bimetal MOFs, other dual metals (e.g., Fe–Co, Ni–Co, Ni–Fe, Cu–Co) are maintained in Zn-free MOF-derived catalysts, which have been demonstrated to possess remarkable ORR catalytic performance (Tang et al., 2016; Guan et al., 2018; Yin et al., 2019; Wang et al., 2020). For instance, $Co_{9-x}Fe_xS_8$/Co,Fe–N–C hybrids wrapped by reduced graphene oxide are synthesized through a semivulcanization and calcination method using graphene oxide-wrapped bimetallic ZIF (Co, Fe-ZIF) as precursors by Liu and co-workers (Liu et al., 2018). Benefiting from the high dispersity and enhanced conductivity, the final catalyst shows a half-wave potential of 0.84 V in ORR, combining a superior oxygen electrode activity of ≈0.68 V in 0.1 M KOH. Besides, the hybrid Ni-based MOF nanosheets decorated with Fe-MOF nanoparticles are synthesized for enhanced water oxidation catalysis under mild conditions by Rui et al. (2018).

Although a lot of ORR catalysts derived from MOFs have been synthesized, there are still several issues in practice: (1) abundant ORR active sites need to be constructed; (2) the influence of metal and doped heteroatom on the structure and composition of MOFs-derived materials need to be explored; and (3) three-dimensional and controllable structure become more important for ORR. The solution to these problems is of great significance to improve the ORR performance of MOFs-derived catalysts, replace the noble metal

catalyst completely, and accelerate the commercialization process of fuel cells.

In this work, a series of carbon-based/metal sulfides composites as efficient ORR catalysts using the tri-MOFs as precursors are produced by a sulfuration–pyrolysis strategy. To address the above-mentioned issues, the Zn/Co/Fe-ZIF (tri-MOFs) is used as the precursor to enrich the active sites. The influences of metal and doped S on the structure and ORR performances of the final material are studied. The structures and morphologies of obtained samples are characterized and analyzed. The ORR activity and durability of obtained samples are systematically compared and evaluated.

MATERIALS AND METHODS

In this section, the details of the preparation of a series of materials derived from MOFs are described, and the subsequent characterization and test methods of the samples are explained.

Chemicals

2-Methylimidazole, potassium hydroxide, cobalt nitrate hexahydrate, zinc nitrate hexahydrate, ferrous sulfate heptahydrate, and sodium sulfide were purchased from Aladdin Company, Shanghai, China. Methanol and ethanol were purchased from Sinopharm Chemical Reagent Co., Ltd. (Shanghai Shi, China) 5% Nafion and commercial 20 wt.% Pt/C were purchased from Johnson Matthey Company, London, United Kingdom. All chemicals were used as received without any further purification. Water deionized (18 MΩ) with a Barnstead E-Pure system (Axiuluo Company, Chongqing, China) was used in all experiments.

Preparation of the Zn/Co/Fe–S–NC Materials

The preparation process of catalysts can be divided into three steps: (1) preparation of MOF precursors by precipitation, (2) formation of sulfides, and (3) carbonization, as shown in **Figure 1**.

First, Zn/Co/Fe-MOFs precursors were prepared by precipitation at room temperature. Then, the metal sulfides were formed by the sulfurization of Zn/Co/Fe-MOFs precursors. Finally, the catalyst materials were obtained by a carbonization process, abbreviated as Zn/Co/Fe–S–NC. For comparison, the obtained Zn/Co/Fe-MOFs were directly carbonized without sulfurization, the obtained samples were abbreviated as Zn/Co/Fe–NC. Besides, the Co/Fe-MOFs were obtained without adding Zn during the first preparation process. The Co/Fe-MOFs precursors were processed the sulfurization and carbonization, and the final products were abbreviated as Co/Fe–S–NC. The detailed preparation process is as follows:

(1) First, Zn/Co/Fe-MOFs precursors were prepared by precipitation at room temperature. About 7.2 mmol $Zn(NO_3)_2{\cdot}6H_2O$, 4.8 mmol $Co(NO_3)_2{\cdot}6H_2O$, and 0.48 mmol $FeSO_4{\cdot}7H_2O$ were dissolved in 100 mL methanol and evenly dispersed to form a bright red solution A. About 48 mmol of 2-methylimidazole were dissolved in 40 mL methanol and evenly dispersed to form a clear solution B. Next, solution A was poured into solution B and was stirred vigorously at room temperature for 0.5 h. After an incubation period of 24 h at room temperature, the final reaction products were washed and dried, marked as Zn/Co/Fe-MOFs. For comparison, $Zn(NO_3)_2{\cdot}6H_2O$ were replaced by $Co(NO_3)_2{\cdot}6H_2O$ at this step, thus, Co/Fe-MOFs can be obtained.

(2) In a typical formation of metal sulfides, 1 g of Zn/Co/Fe-MOFs powder was first dispersed in 250 mL ethanol. Meanwhile, 0.5 g $Na_2S{\cdot}9H_2O$ was evenly dispersed in 50 mL ultrapure water. Then, the water solution was slowly poured into the ethanol solution while stirring for 0.5 h at 85°C. The suspension was centrifuged and washed with ethanol several times and dried.

(3) The metal sulfides were heated to the desired temperature (700–1,100°C) for 2 h under N_2 in a tube furnace to obtain the self-adjusted Zn/Co/Fe–S–NC.

Materials Characterizations and Electrochemical Analysis

The morphologies of obtained samples were observed by field emission scanning electron microscope (FE-SEM, Gemini SEM 500) and high-resolution transmission electron microscope (HR-TEM, JEM-F200). The chemical compositions, crystallographic structures, and valence state of elements were analyzed by X-ray diffraction (XRD, D/max-2500VL/PC, Rigku, Tokyo, Japan) and X-ray photoelectron spectroscopy (XPS, Thermo Fisher Scientific K Alpha, Thermo Fisher Scientific, Waltham, MA, United States). The specific surface area and the pore size distribution were analyzed by Micromeritics ASAP 2460 at 77 K with Barrett–Joyner–Halenda (BJH) and MP models, respectively.

Electrocatalytic measurements were performed with a conventional three-electrode system on an electrochemical

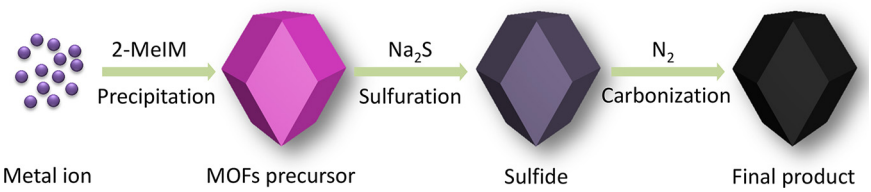

FIGURE 1 | Schematic diagram of the preparation of the Zn/Co/Fe–S–NC catalyst.

workstation (AUTOLAB PGSTAT302N, Metrohm Company, Herisau, Switzerland) at room temperature in 0.1 M KOH solution. A glassy carbon rotating ring disk electrode (GC RRDE, Pine Research Instrumentation, Durham, NC, United States) was used for the working electrode. The Ag/AgCl electrode was used as the reference electrode in 0.1 M KOH solution, respectively. The platinum wire was used as a counter electrode. To prepare the working electrodes, 4-mg catalysts were dispersed in a mixed solution that contained 500 μL ethanol, 500 μL deionizer water, and 45 μL of 5% Nafion solution. It was further disposed by ultrasonic to form a homogeneous catalyst ink. The homogeneous ink was then dropped onto the surface of the working electrode with a loading equivalent of 0.283 mg cm^{-2}. For comparison, commercial Pt/C (20 wt.%, Johnson Matthey) was prepared in the same way. All potentials measured in this work were converted to potential versus RHE. The linear sweep voltammetry (LSV) curves were recorded at scan rates of 5 mV s^{-1} with a rotation speed of 1,600 rpm in both O_2 and N_2 saturated KOH solution. The electron transfer numbers (n) at different potentials varied from 400 to 2,400 rpm were calculated from the Koutecky–Levich (K–L) equation. The durability was conducted in an O_2-saturated condition at 1,600 rpm by chronoamperometric (i–t) response. The initial potential and duration were set at 0.65 V (vs. RHE) and 36,000 s in 0.1 M KOH solution, respectively.

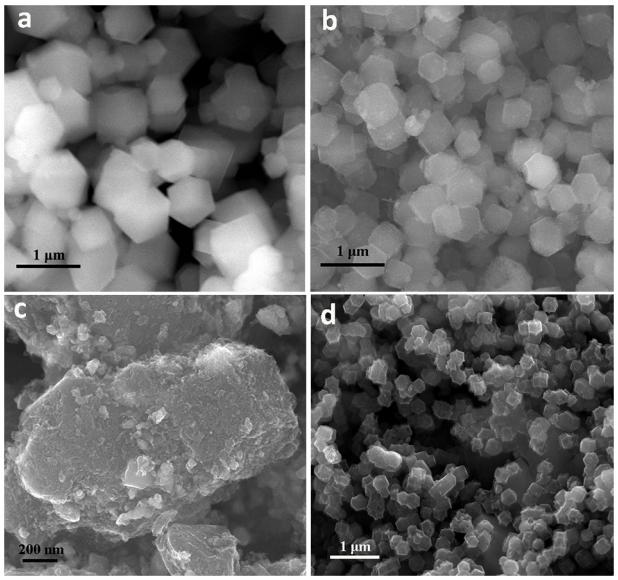

FIGURE 2 | Scanning electron microscope images of **(a)** Zn/Co/Fe-MOF precursor, **(b)** the products after sulfuration, **(c)** the final Zn/Co/Fe–S–NC-900 catalyst, **(d)** the control sample of Zn/Co/Fe–NC-900 without sulfuration.

RESULTS AND DISCUSSION

In this section, first, the structures and micromorphologies of the MOFs-derived precursors, intermediate products, and final Zn/Co/Fe–S–NC catalysts are observed by SEM and TEM, the chemical components and valence state of elements of Zn/Co/Fe–S–NC and control samples are analyzed by XRD and XPS. Next, the porosity and specific surface area are analyzed and determined by Brunner-Emmet-Teller (BET) measurement. Finally, the ORR activity and stability are evaluated, and the future application prospects are envisioned.

Structural and Component Characterizations

The Zn/Co/Fe-MOFs are formed by a coprecipitation reaction of a transition metal nitrate mixture [$Co(NO_3)_2{\cdot}6H_2O$, $Zn(NO_3)_2{\cdot}6H_2O$, $FeSO_4{\cdot}7H_2O$] and 2-methylimidazole at room temperature for 24 h. The obtained precursors remain in the typical rhombododecahedron shape of ZIF-8/ZIF-67, and the uniform particle size is about 500 nm as shown in **Figure 2a**. Next, the precursors are vulcanized by $Na_2S{\cdot}9H_2O$ to achieve S doping. The doping of heteroatom (such as S, P) will change the electron density around the metal–N–C bond, thus realizing the regulation of the electrochemical performance of the materials. After the sulfuration treatment, the surface of the material will become rough, which is the result of the formation of metal sulfides, as shown in **Figure 2b**. The final catalyst material can be obtained by calcining the sulfurized products. During this step, the polymer organic matter, impurities, and water will evaporate. It can be seen that the final material shows a three-dimensional porous structure, as shown in **Figure 2c**. To explore the influence of heteroatom (S) doping on the structure, the morphology of the material directly carbonized without sulfurization was observed, as shown in **Figure 2d**. It can be seen that compared with Zn/Co/Fe–S–NC, the particle size of Zn/Co/Fe–NC is smaller and their surface become smoother. This indicates the successful loading of metal sulfides (Zn–S, Co–S, Fe–S) on 3D carbon nanopolyhedron and the doping of S is conducive to the formation of the porous structure of the material.

Further, the HR-TEM images of Zn/Co/Fe–S–NC-900 are observed, as shown in **Figures 3a–c**. It can be seen that the Co, Fe particles partially wrapped with metal sulfides are uniformly distributed in the carbon nanopolyhedron (CN) matrix. The deep observation of the 3D CN matrix surface indicates the formation of carbon nanotubes (CNTs), seen in **Figure 3a**. At the same time, a clear element mapping image indicates that uniform distributions of C, S, N, Zn, Co, and Fe, as shown in **Figure 3d**.

To further study the chemical composition and structure of the Zn/Co/Fe–S–NC catalyst, XRD patterns of the obtained three samples in **Figure 4** are also tested. First, the diffraction peaks of three samples correspond to Co (JCPDS Card No. 89-7093), which indicates a uniform distribution of cobalt particles in the composites. The peak positions of 44.226°, 51.529°, and 75.863° are indexed to the (1 1 1), (2 0 0), and (2 2 0) planes of Co, respectively. In all samples, two peaks at 25° and 44° can be found, which are assigned to the C (0 0 2) and C (1 0 1). Besides, the planes of Co_3S_4, Fe_7S_8 can be detected, which reveals the chemical composition of Zn/Co/Fe–S–NC composites.

For the material of Zn/Co/Fe–NC-900 (II), at the position of 75.863°, there is no obvious peak. Zn/Co/Fe–NC-900 is obtained by carbonization of MOFs precursor without vulcanization.

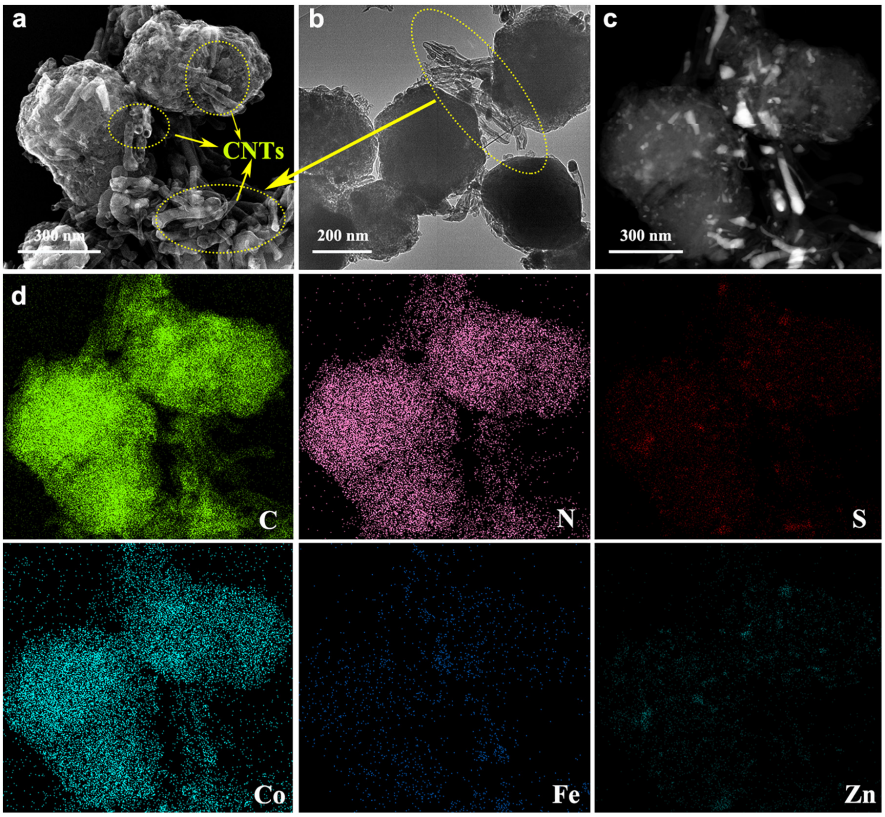

FIGURE 3 | Transmission electron microscopy images of **(a–c)** Zn/Co/Fe–S–NC-900 catalyst and **(d)** the corresponding element mapping images (C, N, S, Co, Fe, Zn).

Therefore, there are no metal sulfides (Co_3S_4, Fe_7S_8) in the material (II). As shown in **Figure 4**, the peak intensities of Zn/Co/Fe–S–NC-900 (I) at 44.226°, 51.529°, and 75.863° are stronger than Zn/Co/Fe–NC-900 (II) and Co/Fe–S–NC-900 (III). This shows that a proper amount of Zn doping is more conducive to the exposure and uniform dispersion of Co particles.

Figure 5 shows the XPS spectra of the Zn/Co/Fe–S–NC and control samples. The valence state of elements, the chemical composition can be further detected. It can be seen that the coexistence of C, N, O, S, Co, Fe, Zn in Zn/Co/Fe–S–NC-900 is confirmed by the XPS survey spectrum in **Figure 5A**. As shown in **Figure 5B**, the high-resolution Zn 2p spectrum can be fitted into two peaks, centered at 1021.6 and 1044.8 eV, which correspond to Zn $2p_{3/2}$ and $2p_{1/2}$ peaks. Evidently, as the temperature increases, the zinc concentration of the material decreases. As shown in **Figure 5B**, when the temperature rises to 900°C, most of the Zn evaporate, but there is still a part of Zn combined with nitrogen in MOFs to form Zn–N. The experimental results show that these Zn–N are extremely beneficial to the stability of the materials. Zn/Co/Fe–S–NC with different temperatures from 700 to 1,100°C are detected by high-resolution spectrum of N1s. In **Figure 5C**, N1s can be separated into five peaks at 397.0–397.6, 398.0–398.6, 399.2–400, 400.5–400.9, and 402.3–403.5 eV, which can be ascribed to the pyridinic-N, pyrrolic-N, M-N_x, graphitic-N, and oxidized-N, respectively. The results show that the content of various kinds of nitrogen in the materials are closely related to the temperature. When the temperature is 700°C,

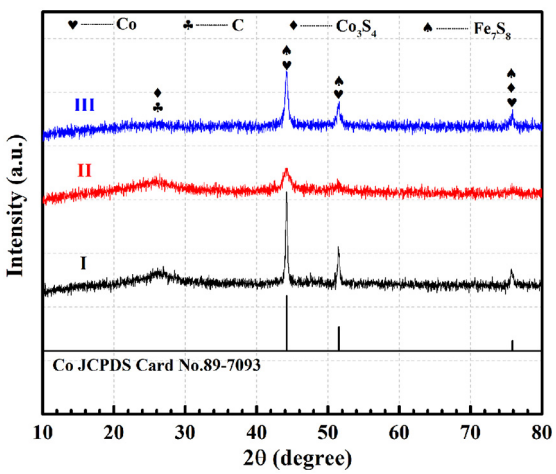

FIGURE 4 | X-ray diffraction spectrum of the Zn/Co/Fe–S–NC-900(I), Zn/Co/Fe–NC-900(II), and Co/Fe–S–NC-900(III).

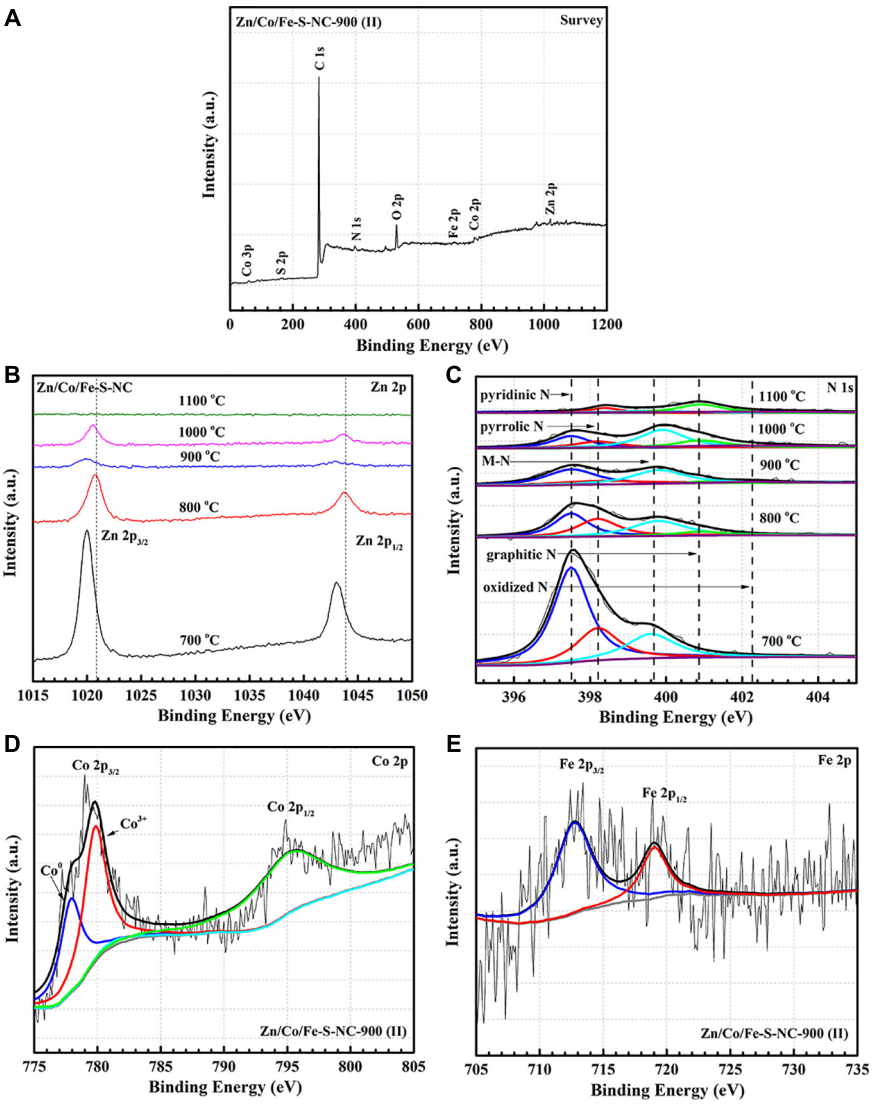

FIGURE 5 | X-ray photoelectron spectroscopy spectra of the Zn/Co/Fe–S–NC and control samples. **(A)** XPS survey scan of Zn/Co/Fe–S–NC-900, **(B)** Zn 2p XPS spectra of Zn/Co/Fe–S–NC with different temperatures (700–1,100°C), **(C)** N 1s XPS spectra of Zn/Co/Fe–S–NC with different temperatures (700–1,100°C), **(D,E)** detailed Co 2p and Fe 2p XPS spectra of Zn/Co/Fe–S–NC-900.

the total nitrogen concentration on the surface of Zn/Co/Fe-S-NC-700 reaches 7.94 at.%, which is higher than that of other samples, as shown in **Supplementary Table 1**. It can be clearly seen that the total nitrogen concentration decreases when the pyrolysis temperature increases from 700 to 1,100°C. This may be due to the loss of pyridinic-N, pyrrolic-N. Conversely, the proportion of graphitic-N and oxidized-N increase gradually, when the temperature rises from 700 to 1,100°C. The contents of different nitrogen species in the resulting samples are determined by XPS (**Supplementary Table 2**). The results show that Zn/Co/Fe–S–NC-900 demonstrates higher concentration of pyridinic-N (41.2 at.%) and M–N (36.8 at.%) with high ORR catalytic activity, significantly better than other catalysts. **Figure 5D** focuses on the high-resolution Co 2p spectrum of Zn/Co/Fe-S-NC-900 catalyst, two signals of Co $2p_{3/2}$, and Co $2p_{1/2}$ are observed. Co $2p_{3/2}$ can be divided into three signals, Co^0 (778.0–778.8 eV), Co^{3+} (779.8–780.4 eV), and Co^{2+} (781.2–782.2 eV). Due to the strong electron-withdrawing effect of N and S, the Co $2p_{3/2}$ peaks in the Zn/Co/Fe–S–NC-900 are positively shifted than those of other catalysts (Zn/Co/Fe–NC-900, Co/Fe–S–NC-900). As shown in **Figure 5E**, the high-resolution Fe 2p spectrum can be fitted into two peaks, centered at 711.2 and 724.6 eV, which correspond to Fe $2p_{3/2}$ and Fe $2p_{1/2}$. This indicates the existence of Fe^{2+} and Fe^{3+} in composites.

With the synergy between transition metal sulfides and NC matrix, CNTs are formed in the surface of carbon matrix. This synergy resulted in the formation of a three-dimensional porous structure, which facilitates the electrons transport. XPS's results indicate the surface concentrations of pyridinic-N and

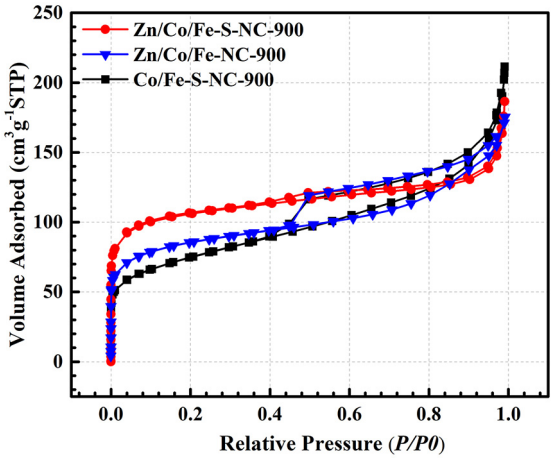

FIGURE 6 | N_2 adsorption/desorption isotherms of Zn/Co/Fe–S–NC-900, Zn/Co/Fe–NC-900, and Co/Fe–S–NC-900.

M–N of the material changes with temperature, and reaches the maximum when the temperature is 900°C.

As shown in **Figure 6**, the porous structures characteristics of samples can be revealed by nitrogen adsorption and desorption isotherms. Obviously, isotherm of type I with an inconspicuous hysteresis loop, indicates the coexistence of the mesoporous and microporous structure. The specific surface area (SSA) of Zn/Co/Fe–S–NC-900, Zn/Co/Fe–NC-900, and Co/Fe–S–NC-900 are 386.75, 306.6, and 258.8 $m^2\ g^{-1}$, respectively. This result indicates that S doping is conductive to formation of porous structure. At the same time, the introduction of Zn in the MOFs precursor is also beneficial to the improvement of porosity. Zn species will promote the increase of SSA and pore volume of the catalysts, but the content of Zn needs to be controlled optimally. Furthermore, the BJH method for mesopores and MP method for micropores are adopted to calculate the range of particle size distribution. The results show that three samples center at ≈1.7 nm (BJH), while micropores mainly center at ≈0.6 nm.

Electrocatalytic ORR Activity in Alkaline Medium

The ORR activities of the as-obtained Zn/Co/Fe–S–NC-900 catalyst are evaluated in 0.1 M KOH solution. The LSV scan rate is set as 5 mV s^{-1}. All potentials measured in this work were converted to potential versus RHE. Equation 1 is used to transform and calculate.

$$\mathrm{E\,(vs.RHE)} = \mathrm{E\left(vs.Ag/AgCl\right)} + 0.0591\mathrm{pH} + 0.197 \quad (1)$$

All measurement experiments are carried out in a typical three-electrode system at ambient temperature. For comparison, the commercially Pt/C catalyst was also measured under identical conditions.

The cyclic voltammetry (CV) curves of the resulting catalysts (Zn/Co/Fe–S–NC-900, Zn/Co/Fe–NC-900, and Co/Fe–S–NC-900) are shown in **Figure 7**. Four catalysts are all present in a rectangular curved shape in an N_2-saturated KOH (0.1 M) solution. This indicates that none of the four materials will undergo catalytic reactions under N_2. As expected, there are obvious ORR cathode peaks in different positions of each catalyst when the KOH solution is aerated with saturated O_2. Further measurements show that Zn/Co/Fe–S–NC-900 has the most positive half-wave potential than other catalysts.

To evaluate the ORR performance of the samples more comprehensively, LSV measurements are performed in O_2-saturated 0.1 M KOH with a sweep speed of 1,600 rpm. First, as shown in **Figure 8A**, the half-wave potentials ($E_{1/2}$) of four samples (Zn/Co/Fe–S–NC-900, Zn/Co/Fe–NC-900, Co/Fe–S–NC-900, Pt/C) are 0.870, 0.837, 0.846, and 0.861 V, respectively. Besides, the limiting current density of Zn/Co/Fe–S–NC-900 is as high as 6.32 mA cm^{-2}. The catalyst of Zn/Co/Fe–S–NC-900 shows the highest ORR catalytic activity among obtained samples, which may be due to the appropriate S and Zn doping.

To study the effect of pyrolysis temperature on electrocatalytic performance of materials, a series of samples are obtained under different temperatures (T = 700, 800, 900, 1,000, 1,100°C). As shown in **Figure 8B**, LSV curves are performed to evaluate the relationship between temperature and ORR performance. Obviously, the catalyst of Zn/Co/Fe–S–NC-900 still shows the highest ORR activity among five typical catalysts. The electrochemical results are also consistent with the XPS's results. At low temperature (700°C), a large amount of Zn cannot be volatilized; thus, the active sites will be covered and the porosity of the materials reduce. At high temperatures (1,000, 1,100°C), a large amount of graphitic-N and oxidized-N will be formed and pyridinic-N and pyrrolic-N will be lost, which is very detrimental to the ORR. Our experimental results prove that the optimal temperature for the formation of ORR active site is 800–900°C.

In the next part, the electron transfer numbers (n) at different potentials varied from 400 to 2,400 rpm are calculated from the K–L equation as shown in Equations 2 and 3:

$$\frac{1}{J} = \frac{1}{J_L} + \frac{1}{J_K} = \frac{1}{B\omega^{1/2}} + \frac{1}{J_K} \quad (2)$$

$$B = 0.62nFC_oD_o^{2/3}V^{-1/6} \quad (3)$$

where J is the measured current density. J_K and J_L are the kinetic and diffusion-limiting current densities, respectively. ω is the rotating speed (revolutions per minute), n is the electron transfer number, F is the Faraday constant (96,485 C mol^{-1}). C_0 is the bulk concentration of O_2 (1.2×10^{-6} mol cm^{-3}). D_0 is the diffusion coefficient of O_2 in the electrolyte (1.9×10^{-5} $cm^2\ s^{-1}$). V is the kinematic viscosity of the electrolyte (0.01 $cm^2\ s^{-1}$).

As shown in **Figure 8C**, with the increase of the RDE rotating speed, the diffusion current density decreases gradually, which may due to the transmission distance between the KOH solution and the ORR active sites. As shown in **Figure 8D**, according to the curve fitting result, it can be clearly seen that Zn/Co/Fe–S–NC-900 is a kind of catalyst with 4-electron transfer mechanism.

The overall kinetics process of the ORR has two main pathways: the 2-electron reduction pathway and a direct 4-electron pathway. According to literature reports (Xu et al.,

TABLE 1 | Comparison of ORR performances of catalysts in this paper with those from literature.

Catalyst	Half-wave potential (V)	Tafel slope (mV dec^{-})	Limiting current density (mA cm^{-2})	Electrolyte	References
Zn/Co/Fe–S–NC-900	0.870	66.0	−6.32	0.1 M KOH	This work
Pt/C	0.861	82.0	−5.46	0.1 M KOH	This work
CoZn–NC-700	0.840	60.0	−4.93	0.1 M KOH	Chen et al., 2017
(Fe,Co)/N–C	0.863	66.0	−6.00	0.1 M $HClO_4$	Wang et al., 2017
$ZnO/ZnCo_2O_4$/C@rGO	0.815	46.7	−5.09	0.1 M KOH	Liu Y. et al., 2017
Ni/CoNC	0.884	–	−5.49	0.1 M KOH	Tang et al., 2016
	0.758	–	−6.46	0.1 M PBS	
Fe–N–C/800-HT2	0.881	68	−5.32	0.1 M KOH	Zhang et al., 2020

2018), the 2-electron reduction process is accompanied by the production of the peroxide species. However, the reduction product of the direct 4-electron transfer process is H_2O, and the energy conversion process is more efficient and faster than the 2-electron process. The electron transfer pathway can be represented as

$$O_2 + H_2O + 2e^- \rightarrow HO_2^- + OH^- \left(\text{Alkaline medium, } 2\ e^- \text{transfer pathway}\right) \quad (4)$$

$$O_2 + 2H_2O + 4e^- \rightarrow 4OH^- \left(\text{Alkaline medium, } 4\ e^- \text{transfer pathway}\right) \quad (5)$$

In this article, at the potential range of 0.3–0.9 V (vs. RHE), the calculated ORR electron-transfer number for Zn/Co/Fe–S–NC-900 is in the range of 3.867–3.956, which indicates that the kinetics process of the ORR calculated by Zn/Co/Fe–S–NC-900 is a 4-electron transfer pathway. The detailed reaction process is as follows: (1) O_2 molecules first diffused and adsorbed to the surface of Zn/Co/Fe–S–NC-900 catalyst. (2) The adsorbed O_2 contacted with active sites of the catalyst, and further combined electrons to produce intermediate products, such as OOH*,OH*,O*. (3) Through a 4 e^- transfer process, adsorbed O_2 was reduced to OH^- on the surface of the active sites under alkaline conditions.

Moreover, Tafel curves of three catalysts and Pt/C are drawn based on the linear region (in low-overpotential region) of LSV curves. As shown in **Figure 8E**, the value of Tafel slope for Zn/Co/Fe–S–NC-900 is lower (66 mV dec^{-1}) than those of Pt/C (82 mV dec^{-1}), Zn/Co/Fe–NC-900 (105 mV dec^{-1}), and Co/Fe–S–NC-900 (98 mV dec^{-1}). The smallest value of the Tafel slope means the fastest kinetic velocity of electron transport, the

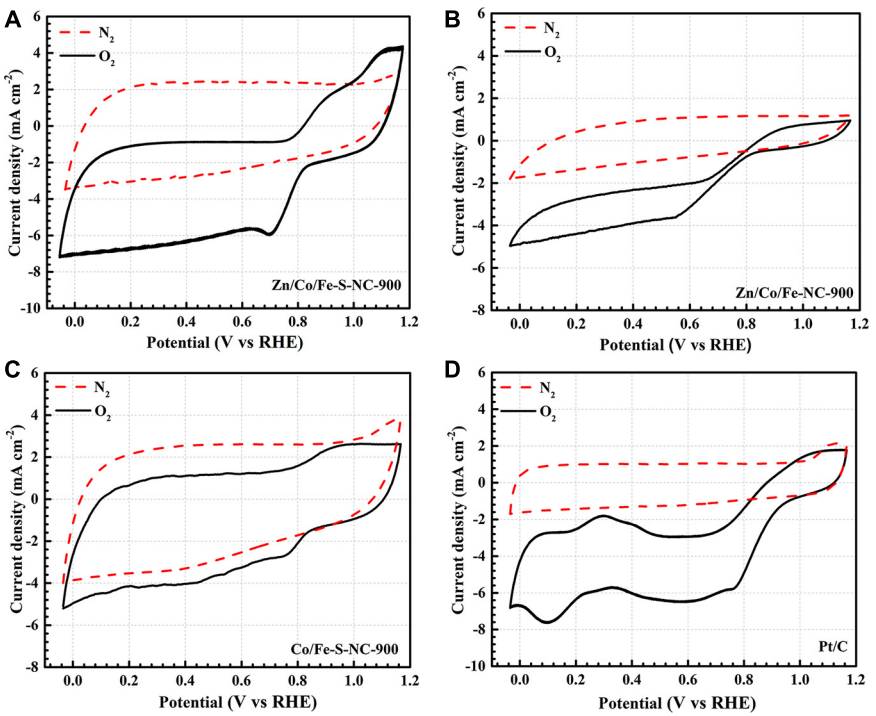

FIGURE 7 | CV curves of the obtained catalysts of **(A)** Zn/Co/Fe–S–NC-900, **(B)** Zn/Co/Fe–NC-900, **(C)** Co/Fe–S–NC-900, **(D)** Pt/C in O_2 and N_2-saturated 0.1 M KOH solution.

smallest activation energy of ORR, and the highest intrinsic ORR activity.

Finally, the long-term stability of the optimal catalyst is evaluated by chronoamperometric (i-t). As shown in **Figure 8F**, the Zn/Co/Fe–S–NC-900 catalyst still retained a 94.1% current rate after 36,000 s, while that of 20% Pt/C was only 88%. The experimental results show that this catalyst has good stability under alkaline conditions.

In summary, three different catalysts are designed and evaluated for ORR. The important role of doped Zn and S are discussed. The optimal catalyst is Zn/Co/Fe–S–NC-900, and its ORR performance is at the leading level among the catalysts developed in recent years, as shown in **Table 1**.

The remarkable performances were mainly attributed to the synergy between transition metal sulfides and NC matrix. This synergy resulted in the formation of a three-dimensional porous structure, which facilitates the electrons transport.

CONCLUSION

In this article, a series of non-precious metal catalytic materials derived from Zn/Co/Fe-MOFs were produced through a sulfuration–calcination treatment. They could be adopted as the efficient ORR catalysts in alkaline media. The structures and morphologies of obtained samples were characterized and analyzed. The influences of metal ratio in MOFs and doped S on the structure and ORR performances of the final materials have been studied through controlled experiments. The effects of process conditions (such as temperature) on structure and performances were also discussed. The ORR activity and durability of obtained samples were systematically compared and evaluated. The main conclusions are as follows:

(1) When the appropriate proportion (Zn and S) were doped in composites, derived catalyst at 900°C (Zn/Co/Fe–S–NC-900) shows the prominent ORR activity and durability with

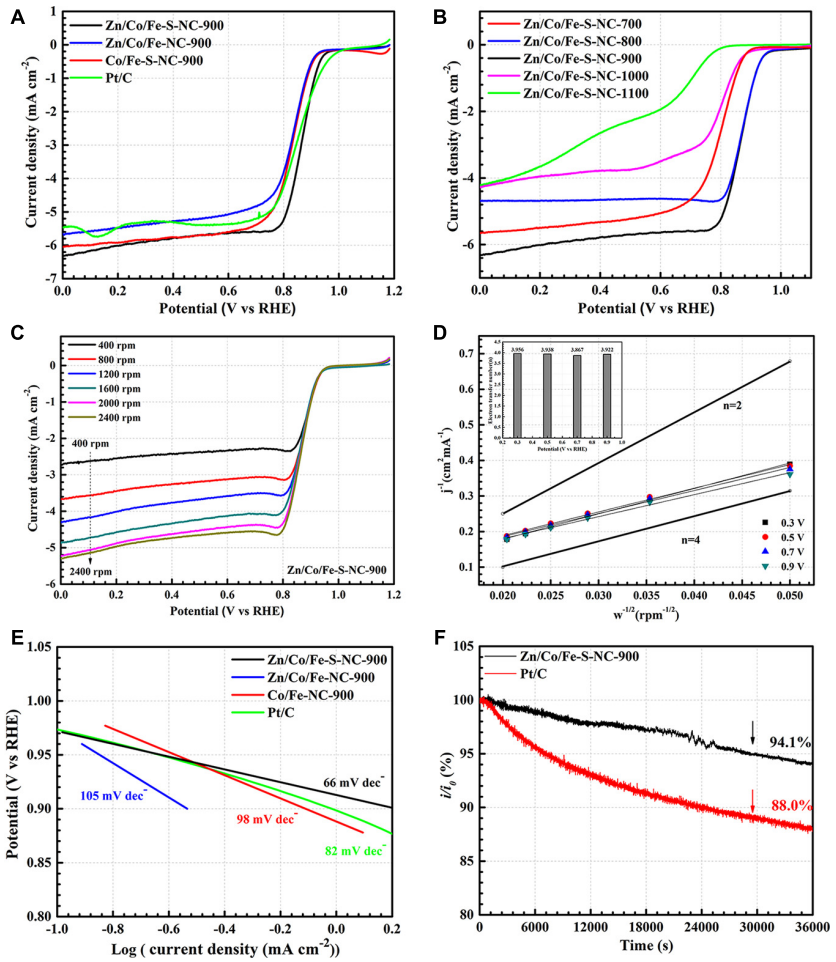

FIGURE 8 | (A) LSV curves of Zn/Co/Fe–S–NC-900, Zn/Co/Fe–NC-900, Co/Fe–S–NC-900, and commercial Pt/C. **(B)** LSV curves of Zn/Co/Fe–S–NC with different temperatures (700–1,100°C). **(C)** LSV curves of the Zn/Co/Fe–S–NC-900 at various rotation rates (400–2,400 rpm) and **(D)** Koutecky–Levich plots at different potentials (illustration: the calculated ORR electron-transfer number from 0.3 to 0.9 V). **(E)** Tafel slopes of Zn/Co/Fe–S–NC-900, Zn/Co/Fe–NC-900, Co/Fe–S–NC-900, and commercial Pt/C from LSV curves at 1,600 rpm. **(F)** Chronoamperometric response of Zn/Co/Fe–S–NC-900 and Pt/C at 0.65 V (vs. RHE). (All LSV curves were conducted on RDE in O_2-saturated 0.1 M KOH solution with scan rate of 5 mV s^{-1} and the rotation rate of 1,600 rpm.)

an $E_{1/2}$ of 0.87 V (vs. RHE) and a J_L of 6.32 mA cm^{-2} in 0.1 M KOH, which are better than those of commercial 20 wt.% Pt/C ($E_{1/2}$ of 0.861 V and J_L of 5.46 mA cm^{-2}). It was proven that this effective catalyst has the potential to replace commercial catalysts in batteries in the future.

(2) The remarkable performances were mainly attributed to the synergy between transition metal sulfides and NC matrix. This synergy resulted in the formation of a three-dimensional porous structure, which facilitates the electron transport.

DATA AVAILABILITY STATEMENT

The original contributions presented in the study are included in the article/**Supplementary Material**, further inquiries can be directed to the corresponding author.

AUTHOR CONTRIBUTIONS

Y-WY and B-YS contributed equally to this article and co-wrote the manuscript. Y-WY conducted the synthesis of the materials. B-YS carried out the characterization and the electrochemical measurements. Both authors contributed equally to this article and co-wrote the manuscript.

FUNDING

This work was financially supported by Natural Science Basic Research Program of Shaanxi (Program No. 2021JQ-510) and the Foundation of Key Laboratory of Thermo-Fluid Science and Engineering (Xi'an Jiaotong University), Ministry of Education, Xi'an 710049, China (KLTFSE2020KFJJ02).

SUPPLEMENTARY MATERIAL

The Supplementary Material for this article can be found online at: https://www.frontiersin.org/articles/10.3389/fenrg.2021.673923/full#supplementary-material

REFERENCES

Chen, B. H., He, X. B., Yin, F. X., Wang, H., Liu, D. J., Shi, R. X., et al. (2017). MO-Co@ N-doped carbon (M=Zn or Co): vital roles of inactive Zn and highly efficient activity toward oxygen reduction/evolution reactions for rechargeable Zn-air battery. *Adv. Funct. Mater.* 27:1700795. doi: 10.1002/adfm.201700795

Chen, Y. Z., Wang, C. M., Wu, Z. Y., Xiong, Y. J., Xu, Q., Yu, S. H., et al. (2015). Metal-organic frameworks: from bimetallic metal-organic framework to porous carbon: high surface area and multicomponent active dopants for excellent electrocatalysis. *Adv. Mater.* 27, 5009–5009. doi: 10.1002/adma.201570229

Cheng, G., Liu, G., Liu, P., Chen, L., Han, S., Han, J., et al. (2019). Nitrogen-doped ketjenblack carbon supported Co3O4 nanoparticles as a synergistic electrocatalyst for oxygen reduction reaction. *Front. Chem.* 7:766. doi: 10.3389/fchem.2019.00766

Chung, H. T., Cullen, D. A., Higgins, D., Sneed, B. T., and Holby, E. F. (2017). Direct atomic-level insight into the active sites of a high-performance PGM-free ORR catalyst. *Science* 357, 479–484. doi: 10.1126/science.aan2255

Fu, S., Zhu, C., Song, J., Du, D., and Lin, Y. (2017). Metal-organic framework-derived non-precious metal nanocatalysts for oxygen reduction reaction. *Adv. Energy Mater.* 7:1700363. doi: 10.1002/aenm.201700363

Guan, B. Y., Lu, Y., Wang, Y., Wu, M. H., and Lou, X. W. (2018). Porous iron-cobalt alloy/nitrogen-doped carbon cages synthesized via pyrolysis of complex metal-organic framework hybrids for oxygen reduction. *Adv. Funct. Mater.* 28:1706738. doi: 10.1002/adfm.201706738

Guo, Z. Y., Wang, F. M., Xia, Y., Li, J., Tamirat, A. G., Liu, Y., et al. (2018). In situ encapsulation of core-shell-structured Co@ Co3O4 into nitrogen-doped carbon polyhedra as a bifunctional catalyst for rechargeable Zn-air batteries. *J. Mater. Chem. A* 6, 1443–1453. doi: 10.1039/c7ta09958d

Hu, H., Han, L., Yu, M., Wang, Z., and Lou, X. W. (2016). Metal-organicframework-engaged formation of Co nanoparticle-embedded carbon@Co9S8 double-shelled nanocages for efficient oxygen reduction. *Energy Environ. Sci.* 9, 107–111. doi: 10.1039/c5ee02903a

Katsounaros, I., Cherevko, S., Zeradjanin, A. R., and Mayrhofer, K. J. (2014). Oxygen electrochemistry as a cornerstone for sustainable energy conversion. *Angew. Chem. Int. Ed.* 53, 102–121. doi: 10.1002/anie.201306588

Li, R., Dai, Y., Chen, B., Zou, J., Jiang, B., and Fu, H. (2016). Nitrogen-doped Co/Co9S8/partly-graphitized carbon as durable catalysts for oxygen reduction in microbial fuel cells. *J. Power Sour.* 307, 1–10. doi: 10.1016/j.jpowsour.2015.12.115

Liu, B., Shioyama, H., Akita, T., and Xu, Q. (2008). Metal-organic framework as a template for porous carbon synthesis. *J. Am. Chem. Soc.* 130, 5390–5391. doi: 10.1021/ja7106146

Liu, S. W., Tong, M. Y., Liu, G. Q., Zhang, X., Wang, Z., Wang, G., et al. (2017). S, N-Containing Co-MOF derived Co9S8@S, N-doped carbon materials as efficient oxygen electrocatalysts and supercapacitor electrode materials. *Inorg. Chem. Front.* 4, 491–498. doi: 10.1039/c6qi00403b

Liu, T., Yang, F., Cheng, G., and Luo, W. (2018). Reduced graphene oxide-wrapped Co9-xFexS8/Co,Fe-N-C composite as bifunctional electrocatalyst for oxygen reduction and evolution. *Small* 14:1703748. doi: 10.1002/smll.201703748

Liu, Y., Jiang, H., Hao, J., Liu, Y., Shen, H., Li, W., et al. (2017). Metal-organic framework-derived reduced graphene oxide-supported ZnO/ZnCo2O4/C hollow nanocages as cathode catalysts for aluminum-O2 batteries. *ACS Appl. Mater. Inter.* 9, 31841–31852. doi: 10.1021/acsami.7b08647

Luo, X., Han, W. L., Ren, H., and Zhuang, Q. Z. (2019). Metallic organic framework-derived Fe, N, S co-doped carbon as a robust catalyst for the oxygen reduction reaction in microbial fuel cells. *Energies* 12:3846. doi: 10.3390/en12203846

Qi, C. L., Zhang, L., Xu, G. C., Sun, Z., Zhao, A., and Jia, D. (2018). Co@Co3O4 nanoparticle embedded nitrogen-doped carbon architectures as efficient bicatalysts for oxygen reduction and evolution reactions. *Appl. Surf. Sci.* 427, 319–327. doi: 10.1016/j.apsusc.2017.08.209

Rui, K., Zhao, G., Chen, Y., Lin, Y., Zhou, Q., Chen, J., et al. (2018). Hybrid 2D dual-metal-organic frameworks for enhanced water oxidation catalysis. *Adv. Funct. Mater.* 28:1801554. doi: 10.1002/adfm.201801554

Shabani, M., Younesi, H., Rahimpour, A., Rahimnejad, M., and Zinatizadeh, A. (2020). A critical review on recent proton exchange membranes applied in microbial fuel cells for renewable energy recovery. *J. Clean Prod.* 264:121446. doi: 10.1016/j.jclepro.2020.121446

Tang, H. L., Cai, S. C., Xie, S. L., Wang, Z. B., Tong, Y. X., Pan, M., et al. (2016). Metal-organic-framework-derived dual metal- and nitrogen-doped carbon as efficient and robust oxygen reduction reaction catalysts for microbial fuel cells. *Adv. Sci.* 3:1500265. doi: 10.1002/advs.201500265

Tang, J., Salunkhe, R. R., Liu, J., Torad, N. L., Imura, M., Furukawa, S., et al. (2015). Thermal conversion of core-shell metal-organic frameworks: a new method for selectively functionalized nanoporous hybrid carbon. *J. Am. Chem. Soc.* 137, 1572–1580. doi: 10.1021/ja511539a

Wang, J., Huang, Z. Q., Liu, W., Chang, C., Tang, H., Li, Z., et al. (2017). Design of N-coordinated dual-metal sites: a stable and active Pt-free catalyst for acidic

oxygen reduction reaction. *J. Am. Chem. Soc.* 139, 17281–17284. doi: 10.1021/jacs.7b10385

Wang, L., Wen, B., Bai, X., Liu, C., and Yang, H. (2019). Facile and green approach to the synthesis of zeolitic imidazolate framework nanosheet-derived 2D Co/C composites for a lightweight and highly efficient microwave absorber. *J. Colloid Interface Sci.* 540, 30–38. doi: 10.1016/j.jcis.2018.12.111

Wang, Y., Zhong, K. Q., Huang, Z. Y., Chena, L., Dai, Y., Zhang, H., et al. (2020). Novel g-C3N4 assisted metal organic frameworks derived high efficiency oxygen reduction catalyst in microbial fuel cells. *J. Power Sour.* 450:227681. doi: 10.1016/j.jpowsour.2019.227681

Xia, B. Y., Yan, Y., Li, N., Wu, H. B., Lou, X. W., and Wang, X. (2016). A metal-organic framework-derived bifunctional oxygen electrocatalyst. *Nat. Energy* 1:15006.

Xu, P., Zhang, J., Jiang, G., Hassan, F., Choi, J. Y., Fu, X., et al. (2018). Embellished hollow spherical catalyst boosting activity and durability for oxygen reduction reaction. *Nano Energy* 51, 745–753. doi: 10.1016/j.nanoen.2018.07.031

Yin, M. Y., Zhang, Y. Y., Bian, Z. F., Bu, Y. F., Chen, X. Y., Zhu, T. L., et al. (2019). Efficient and stable nanoporous functional composited electrocatalyst derived from Zn/Co-bimetallic zeolitic imidazolate frameworks for oxygen reduction reaction in alkaline media. *Electrochim. Acta* 299, 610–617. doi: 10.1016/j.electacta.2018.12.171

You, B., Jiang, N., Sheng, M., Drisdell, W. S., Yano, J., and Sun, Y. J. (2015). Bimetal-organic framework self-adjusted synthesis of support-free nonprecious electrocatalysts for efficient oxygen reduction. *ACS Catal.* 5, 7068–7076. doi: 10.1021/acscatal.5b02325

Yu, L., Hu, H., Wu, H. B., and Lou, X. W. (2017). Complex hollow nanostructures: synthesis and energy-related applications. *Adv. Mater.* 29:1604563. doi: 10.1002/adma.201604563

Yu, X., Yu, L., and Lou, X. W. (2016). Metal sulfide hollow nanostructures for electrochemical energy storage. *Adv. Energy Mater.* 6:1501333. doi: 10.1002/aenm.201501333

Zhang, G. Q., Li, L., Chen, M. Y., and Yang, F. L. (2020). Chitosan cross-linked poly (aminoanthraquinone)/ Prussian blue ternary nitrogen precursor-derived Fe-N-C oxygen reduction catalysts for microbial fuel cells and zinc-air batteries. *J. Mater. Chem. A* 8:9256. doi: 10.1039/d0ta00306a

Zhang, J., Zhao, Z., Xia, Z., and Dai, L. (2015). A metal-free bifunctional electrocatalyst for oxygen reduction and oxygen evolution reactions. *Nat. Nanotechnol.* 10:444. doi: 10.1038/nnano.2015.48

Zhang, L. H., Hu, Y. Y., Chen, J. F., Huang, W. T., Cheng, J. H., and Chen, Y. C. (2018). A novel metal organic framework-derived carbon-based catalyst for oxygen reduction reaction in a microbial fuel cell. *J. Power Sourc.* 384, 98–106. doi: 10.1016/j.jpowsour.2018.02.078

Zhao, Y., Nakamura, R., Kamiya, K., Nakanishi, S., and Hashimoto, K. (2013). Nitrogen-doped carbon nanomaterials as non-metal electrocatalysts for water oxidation. *Nat. Commun.* 4:2390.

Zhong, H. X., Wang, J., Zhang, Y. W., Xu, W. L., Xing, W., Xu, D., et al. (2014). ZIF-8 derived grapheme-based nitrogen-doped porous carbon sheets as highly efficient and durable oxygen reduction electrocatalysts. *Angew. Chem. Int. Ed.* 53, 14235–14239. doi: 10.1002/anie.201408990

Zhu, Z., Yang, Y., Guan, Y., Xue, J., and Cui, L. (2016). Construction of a cobalt-embedded nitrogen-doped carbon material with the desired porosity derived from the confined growth of MOFs within graphene aerogels as a superior catalyst towards HER and ORR. *J. Mater. Chem. A* 4, 15536–15545. doi: 10.1039/c6ta05196k

Conflict of Interest: The authors declare that the research was conducted in the absence of any commercial or financial relationships that could be construed as a potential conflict of interest.

The handling editor declared a shared affiliation with the authors at time of review.